Pattern Formation in Taylor-Couette Flow of Dilute Polymer Solutions: Dynamical Simulations and Mechanism

D. G. Thomas, R. Sureshkumar,* and B. Khomami

Department of Chemical Engineering and the Center for Materials Innovation, Washington University, St. Louis, Missouri 63130, USA

(Received 20 April 2006; published 1 August 2006)

We report spatiotemporal pattern formation in Taylor-Couette flow (i.e., flow between rotating cylinders) of viscoelastic dilute polymer solutions obtained for the first time from first-principles dynamical simulations. Solution structures with varying spatial and temporal symmetries, such as rotating standing waves, flames, disordered oscillations, and solitary vortex solutions which include diwhirls (stationary and axisymmetric) and oscillatory strips (axisymmetric or nonaxisymmetric), are observed, depending on the ratio of fluid relaxation time to the time period of inner cylinder rotation. The flow-microstructure coupling mechanisms underlying the pattern formation process are also discussed.

DOI: 10.1103/PhysRevLett.97.054501 PACS numbers: 47.54.−r, 47.20.Ky, 47.20.Qr, 47.57.Ng

Understanding the flow-microstructure coupling leading to nonlinear pattern formation in viscoelastic fluids is of fundamental and technological interest. For instance, such knowledge can be used advantageously in the design and control of polymer processing operations allowing for higher throughput and high product quality, polymer-induced turbulent drag reduction, i.e., the dramatic reduction of turbulent skin friction obtained by the dissolution of minute amounts of high molecular weight polymers, and advanced materials synthesis (e.g., polymer-clay composites). Moreover, a series of flow transitions could be induced by the nonlinear coupling between flow and conformation, leading to phenomenon such as elastic turbulence [1], i.e., chaotic flows with spectral energy transfer realized in the absence of inertia. Specifically, it is well known that viscoelastic shear flows with curved streamlines are prone to instabilities even in the absence of inertia due to the development of hoop (normal) stresses. The primary elastic instability mechanism was originally established by Larson, Shaqfeh, and Muller [2] for the Taylor-Couette flow (TCF), i.e., the flow generated within the gap of concentric cylinders (with length $\gg$ gap width) by the rotation of the inner cylinder, via a linear stability analysis using a model that mimics the rheology of a highly elastic, constant viscosity dilute polymer solution (Boger fluid) used in their experiments. Since then, as in the Newtonian fluid mechanics literature, TCF has served as a paradigm for investigations of elastic instabilities and pattern formation. Experimental investigations of pattern formation in viscoelastic TCF have uncovered a variety of intriguing flow transitions, including rotating standing waves (RSW), disordered oscillations (DO), and solitary vortex solutions which can be time dependent [oscillatory strips (OS)] or time invariant [diwhirls (DW)] [3]. However, to date, theoretical investigations have been limited to weakly nonlinear analysis [4] or computation of axisymmetric steady states [5]. This has limited the understanding of the mechanisms of flow-microstructure coupling underlying the pattern formation process, which, as shown by experiments, inherently includes creation or destruction of spatial (i.e., axisymmetry vs nonaxisymmetry, periodicity in the direction of the cylinder axis) and temporal (i.e., stationary, time periodic, or disordered) symmetries which can be captured only by means of a fully three-dimensional dynamical simulation. In this Letter, we report, for the first time, the principal findings of such dynamical explorations and discuss the pattern formation mechanisms.

The ratio of inertial to elastic forces plays an important role in polymer solution flows. This ratio is referred to as the elasticity number, $E \equiv \mathrm{We}/\mathrm{Re}$, where Re and We denote the Reynolds (ratio of inertial to viscous forces) and Weissenberg (ratio of fluid relaxation time λ to the inverse of the characteristic shear rate $\dot{\gamma}$) numbers, respectively. In the limit as $E \rightarrow \infty$ and under isothermal conditions [6], the base unidirectional Couette flow becomes unstable to a nonaxisymmetric and time-dependent state when the parameter $K \equiv \mathrm{We}^2(1-\beta)(d/R_1)$ exceeds an $O(1)$ critical value where $d \equiv R_2 - R_1$, R_1 and R_2 correspond to the inner and outer cylinder radii, respectively, and β is the solvent to the solution viscosity ratio. The above result has been verified experimentally by Groisman and Steinberg [3], who also provided detailed experimental reports of a variety of patterns that emerge in the postcritical regime. These elastically induced flow patterns, identified as RSW, DO, OS and DW, form for a wide range of conditions ranging from inertia-dominated ($E < 1$) to elasticity-dominated ($E \gg 1$) flows. While the disordered oscillations have been closely associated with the phenomenon of ''elastic turbulence'' [1], the stationary, axisymmetric, and spatially localized coherent structures referred to as ''diwhirls'' [3,7] could exist even below the We threshold of stability of the base Couette flow predicted by linear stability analysis. Experiments [3] suggested that flows resulting from the evolution of finite-amplitude perturbations (which cannot be accounted for by linear stability analysis) could exhibit spatial features of DW. Independent experiments by Baumert and Muller [8]

have shown patterns such as flames made up of DW-like coherent structures to exist at low and high E values.

Direct computation of the viscoelastic flow patterns has remained a formidable challenge due to algorithmic and computational bottlenecks [9]. Kumar and Graham [5] computed axisymmetric and stationary solutions of the DW type by tracing out stationary branches in the purely elastic ($E \to \infty$) Couette-Dean flow using 2D steady state calculations and provided a self-sustaining mechanism that supports the DW structure. Recently, we have developed and extensively validated an efficient, fully spectral, three-dimensional, parallel algorithm, based on the modification of the operator splitting, diffusive-stress formulation used in direct numerical simulation of viscoelastic turbulent flows [10], for the computation of nonaxisymmetric and time-dependent viscoelastic flow structures [9]. It has been shown that consistent with the results of local nonlinear analysis [4], RSW (ribbon) and spiral patterns manifest for We values slightly greater than the linear stability threshold, We_c [9]. In this study, we have employed this algorithm to uncover TCF patterns for $\mathrm{We} \gg \mathrm{We}_c$. We have used the FENE-P (finitely extensible nonlinear elastic-Peterlin) constitutive equation to model the viscoelastic stress. This model is inspired by polymer kinetic theory and is based on a finitely extensible dumbbell realization of a polymer chain in which the two Brownian beads are connected by a nonlinear entropic spring. Despite its simplicity, this model has been successfully used to predict complex phenomena such as polymer-induced turbulent drag reduction [10,11] as well as in the study of viscoelastic coherent structures [5,12]. We choose d, $d/(R_1\Omega)$, $R_1\Omega$, $\rho(R_1\Omega)^2$, and $\eta_P R_1\Omega/d$ as scales for length, time, velocity $\boldsymbol{u}$, pressure p, and polymer stress $\boldsymbol{\tau}$, respectively, where Ω denotes the inner cylinder angular velocity, ρ represents the solution density, and the total solution viscosity η is the sum of the solvent (η_S) and polymeric (η_P) contributions. Further we scale the conformation tensor $\boldsymbol{C}$, which represents the ensemble average of the second moment of the end-to-end vector of the polymer chain, with respect to kT/H, where k, T, and H denote the Boltzmann constant, absolute temperature, and Hookean spring constant, respectively. Then the dimensionless equations governing the motion of an incompressible FENE-P fluid can be expressed as follows [13]:

$$\frac{\partial \boldsymbol{u}}{\partial t} + \boldsymbol{u}\cdot\boldsymbol{\nabla}\boldsymbol{u} = -\boldsymbol{\nabla}p + \frac{\beta}{\mathrm{Re}}\boldsymbol{\nabla}^2\boldsymbol{u} + \frac{(1-\beta)}{\mathrm{Re}}\boldsymbol{\nabla}\cdot\boldsymbol{\tau}, \quad (1)$$

and

$$\frac{\partial \boldsymbol{C}}{\partial t} = -\boldsymbol{u}\cdot\boldsymbol{\nabla}\boldsymbol{C} + \boldsymbol{C}\cdot\boldsymbol{\nabla}\boldsymbol{u} + (\boldsymbol{\nabla}\boldsymbol{u})^T\cdot\boldsymbol{C} - \boldsymbol{\tau}, \quad (2)$$

where $\boldsymbol{\tau} = \{[(L^2-3)/(L^2-\mathrm{trace}(\boldsymbol{C}))]\boldsymbol{C} - \boldsymbol{I}\}/\mathrm{We}$. Note that $\mathrm{trace}(\boldsymbol{C}) < L^2$, $\mathrm{Re} = \rho R_1\Omega d/\eta$, and $\mathrm{We} = \lambda R_1\Omega/d$. The equations are supplemented by no slip boundary conditions at the walls.

We use a large value for $L^2 = 10\,000$ and $\beta = 0.8$ for which the solution has shear-independent viscosity as in the case of the fluids used in experiments. Motivated by experiments, we report results for a moderate value of $E = 1/3$ and $R_1/R_2 = 0.8$ for which computational cost is reasonable (typical CPU time per run is several days on a 16 processor SGI Origin). For this case, linear stability analysis predicts critical values of We, Re, α (axial wave number scaled with respect to $1/d$), and ξ (azimuthal wave number) as 11.44, 34.33, 4.4, and 1, respectively. First, dynamical simulations are performed for $\mathrm{We} = 13$ using the initial condition constructed by the superposition of the base Couette flow with suitably weighted eigenfunctions obtained from linear stability analysis [9]. In discrete steps between 0.5 and 5, we incremented We to a value of 30 and subsequently decreased it from 30 to the linear stability threshold by keeping E fixed at $1/3$. We note that step size has no effect on the flow states reported. Going upward or downward in We at fixed elasticity number is equivalent to increasing or decreasing the shear rate (or Ω in experiments), since E is independent of $\dot{\gamma} \equiv R_1\Omega/d$. For each We value, the simulations are performed for a sufficiently long time [typically of $O(100\lambda)$] and the final solution is used as an initial condition to the simulation at the next We value. The patterns are visualized by using space-time plots for radial velocity (u_r), which convey dynamical information based on pointwise velocity data in Fig. 1. The data are sampled at time intervals of $5\lambda/\mathrm{We}$ [$\equiv 5d/(R_1\Omega)$] units along an axial (z) line passing through the center of the computational domain, i.e., at $r = (R_1 + R_2)/2d$ and $\theta = \pi$. In gray scale, the dark and light regions correspond to radial inflow and outflow regions, respectively. In order to elucidate the flow-microstructure coupling mechanisms, we also present the contour plots in the r-z plane of u_r and trace($\boldsymbol{C}$) in Figs. 2(a) and 2(b), respectively. The RSW pattern in Fig. 1(a) is distinguishable from its checkerboardlike feature that signifies alternating regions of radial inflow (dark) and outflow (light) similar to the ones observed in experiments [3]. The time periods of the fluctuating radial velocity were found to be much greater than the fluid relaxation time and were approximately 43λ and 63λ for $\mathrm{We} = 13$ and 20 [see Fig. 1(a)], respectively. In an ideal RSW a pair of counterrotating vortices of equal sizes generates radial inflow and outflow. However, a distinct asymmetry between the inflow and outflow is visible in the RSW-like patterns shown in Fig. 2(a). This radial asymmetry is reinforced further as We is increased where the flow patterns appear as modulated RSW [see Figs. 1(b) and 2(a)]. For $\mathrm{We} = 30$, regions of strong inflow become further accentuated in the radial and azimuthal directions and the flow manifests as axisymmetric strips of oscillating inflow regions or OS as shown in Figs. 1(c) and 2(a). The inflow radial velocity in the OS was found to oscillate at a frequency $= 1/(5.63\lambda)$ within an axial distance of 0.91 times the gap width. Small random perturbations render the axisymmetric OS solutions

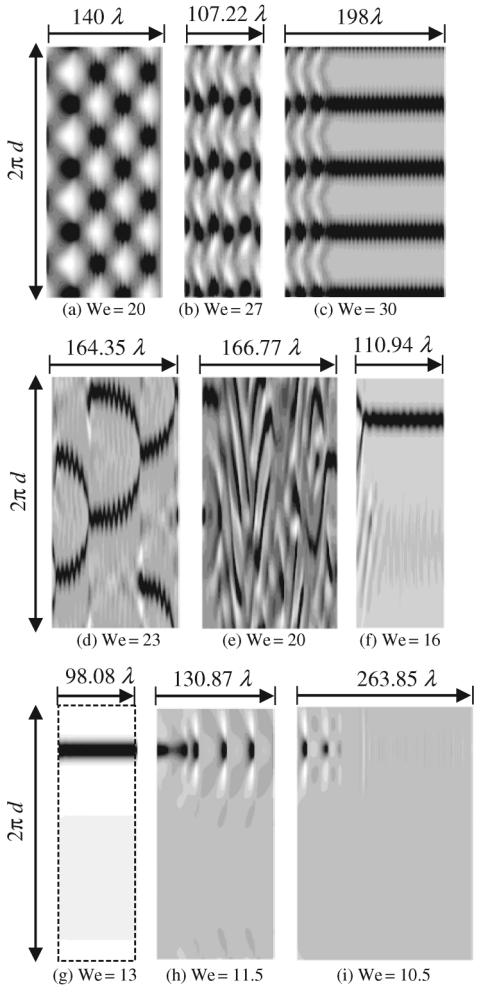

FIG. 1. Space-time plots of radial velocity for (a) RSW, (b) modulated RSW, (c) axisymmetric OS, (d) nonaxisymmetric OS or flames, (e) DO, (f) axisymmetric OS, (g) axisymmetric and stationary DW, (h) diwhirl deteriorating phase, and (i) transition to Couette flow.

unstable to disordered nonaxisymmetric OS at We = 30. The oscillating inflow vortices appear as merging and diverging strips as they are convected azimuthally and axially and the merging or diverging events become more regular and periodic when the We is decreased from 30 to values of 28, 26, and 23 [Fig. 1(d)]. These are reminiscent of the flame patterns reported in the experiments of Baumert and Muller (see Figs. 26 and 10 in the two references, respectively, of [8]) and also resemble the coalescence of two solitary, localized coherent structures of the stationary diwhirls [see Fig. 2(a)] observed in the experiments by Groisman and Steinberg (see Fig. 6 in their paper [7]). Decreasing We from 23 to 20 resulted in an abrupt transition to a disordered flow as shown in Fig. 1(e), whose irregular patterns are similar to those of experimentally observed DO at relatively low elasticity numbers. Sporadic occurrences of spiral- and ribbonlike patterns are also seen in this flow regime. The power spectral

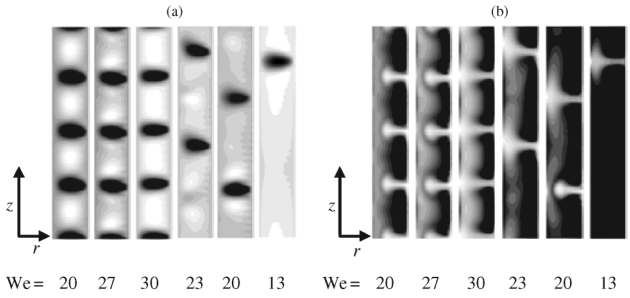

FIG. 2. Final snapshot of r-z contour density plots at an azimuthal point where radial inflow velocity is the maximum: (a) radial velocity V_r and (b) trace($\boldsymbol{C}$) for RSW (We = 20), modulated RSW (We = 27), axisymmetric OS (We = 30), flames (We = 23), DO (We = 20), and DW (We = 13). For each r-z plot, $0 \le z \le 2\pi$, $R_1/d \le r \le R_2/d$.

densities of both the radial and axial velocity fluctuations showed power-law decay behavior with an exponent of -3. At We = 16, flow transitions into an axisymmetric, oscillating, and solitary structure characterized by regions of strong inflow [Fig. 1(f)]. Below We = 16, stationary ringlike (axisymmetric) solitary, localized vortex pairs, or DW emerge as shown in Fig. 1(g). In accord with experimental findings [7], the DW dissipate and transition eventually into unidirectional Couette flow [see Figs. 1(h) and 1(i)] below We $\cong$ 10, which is less than We$_c$.

The maximum value of the radial velocity scaled with respect to d/λ, denoted by V_r, in the inflow of a DW is of $O(1)$ and occurs always at a radial position that is closer to the outer cylinder. Moreover, the strong inflow regions are always associated with large polymer extensions, signified by large values of trace ($\boldsymbol{C}$), as clearly evident from Fig. 2(b). The dark regions in Fig. 2(a) correspond to very intense inward flow in the middle of two vortices, which together are shaped like a spindle [Fig. 3(a)], and the major portion of the flow outside of the DW resembles Couette flow. Flow streamlines in the DW for We = 13, presented in Fig. 3(a), are strikingly similar to the schematic of the flow lines reported from experiments ($\beta = 0.55$, We $\approx$ 10) [7] as well as computed [5] DW structures in the purely elastic case ($E \gg 1$). For the stationary pattern at We = 13, the magnitude of the maximum inflow velocity is $0.652d/\lambda$ compared to $0.5d/\lambda$ from laser Doppler velocimetry measurements [7], and this is nearly 7 times the maximum outflow velocity [Fig. 3(b)]. The axial span of the intense inflow is approximately $0.62d$, while the slower outflow extends nearly $2.75d$ on either side of the inflow core. Corresponding inflow and outflow axial widths reported in experiments [7] were $0.5d$ and $2.5d$, respectively, which are in close agreement with the above predictions that are obtained using a computational domain with an axial height of $2\pi d$. Experiments [7] show that when any two DW approach within an axial range of $5d$, they tend to coalesce to form a single DW. This coalescence feature was also exhibited by the flame pat-

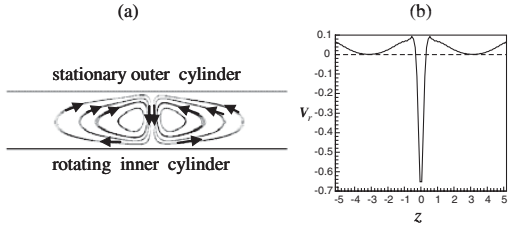

FIG. 3. (a) Flow streamlines in a diwhirl core for We = 13 and (b) V_r vs axial distance in the diwhirl core where V_r is maximally negative for We = 13.

terns of Fig. 1(d) from the present study. In the inflow regions, the mean azimuthal velocity, u_θ, exhibits a parabolic profile near the outer wall. The radial component of the polymer body force, $F_r \equiv [(1-\beta)/\mathrm{Re}\nabla\cdot\boldsymbol{\tau}]_r$, shown in Fig. 4, can be seen to be negative throughout the gap and attains its maximum absolute value near the outer cylinder. This body force, which is generated due to the flow-induced stretching of the polymers, in turn sustains the inward flow.

In summary, in this Letter, we have reported elastically induced flow patterns such as RSW, modulated RSW, axisymmetric OS, flames or nonaxisymmetric OS, DO, and stationary axisymmetric DW computed via 3D time-dependent simulations using a FENE-P model at an elasticity number of 1/3. Since the solution elasticity $E = 1/3$, there is a significant amount of inertia in the above discussed flows; however, the ratio $\mathrm{Re}/\mathrm{Re}_0$ (Re_0 is the critical Reynolds number at which the base Newtonian Couette flow becomes unstable to Taylor-vortex flow) is less than unity ($0.33 \leq \mathrm{Re}/\mathrm{Re}_0 \leq 0.95$). Moreover, parametric studies have shown that the solitary solution structures (OS, DW) can be observed at similar We values even for purely elastic flows ($E \rightarrow \infty$). Hence, the pattern formation reported here can be primarily attributed to elastic effects. Slightly above the critical point predicted by linear stability analysis RSW (ribbons), which are periodic in space and time, manifest. Perturbation of RSW leads to asymmetry between the inflow and outflow regions. The macromolecular extension caused by such flows results in negative (inwardly acting) polymer body force, which in turn reinforces the inflow regions leading to localized vortex solutions with varying spatiotemporal symmetries. The presence of localized coherent structures (DW, OS) with pronounced radial inflow/outflow asymmetry is a common feature exhibited by these flows as previously suggested by the experiments of Groisman and Steinberg [3].

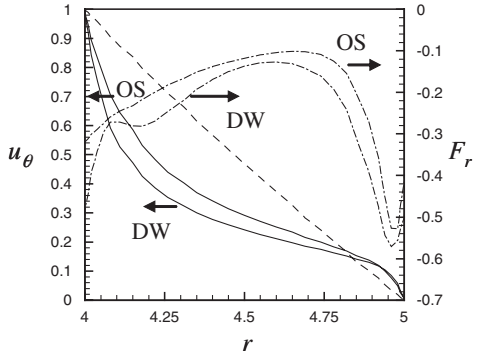

FIG. 4. Azimuthal velocity u_θ and radial polymer body force F_r vs gap radius in the inflow region (where V_r is maximally negative) of an axisymmetric OS (We = 30) and DW (We = 13).

The authors gratefully acknowledge the NSF for the financial support of this research through Grant No. CTS-0335348 and the CSPC (Washington University) for computational resources.

*Electronic address: suresh@che.wustl.edu

[1] A. Groisman and V. Steinberg, Nature (London) **405**, 53 (2000); New J. Phys. **6**, 29 (2004); R. G. Larson, Nature (London) **405**, 27 (2000).

[2] R. G. Larson, E. S. G. Shaqfeh, and S. J. Muller, J. Fluid Mech. **218**, 573 (1990); E. S. G. Shaqfeh, Annu. Rev. Fluid Mech. **28**, 129 (1996).

[3] A. Groisman and V. Steinberg, Phys. Fluids **10**, 2451 (1998); Phys. Rev. Lett. **77**, 1480 (1996); V. Steinberg and A. Groisman, Philos. Mag. B **78**, 253 (1998).

[4] R. Sureshkumar, A. N. Beris, and M. Avgousti, Proc. R. Soc. A **447**, 135 (1994).

[5] K. A. Kumar and M. D. Graham, Phys. Rev. Lett. **85**, 4056 (2000); J. Fluid Mech. **443**, 301 (2001).

[6] Dilute solutions of high molecular weight polymers with thermal sensitive viscosity are susceptible to thermoelastic instabilities in the presence of viscous heating. Secondary flow is axisymmetric and stationary, and linear onset Weissenberg number values could be an order of magnitude lower compared to those in the isothermal case. The isothermal limit is realized when the fluid relaxation time is much greater than the thermal diffusion time scale based on the gap width. See U. A. Al-Mubaiyedh, R. Sureshkumar, and B. Khomami, Phys. Fluids **11**, 3217 (1999); J. Rheol. (N.Y.) **44**, 1121 (2000); Phys. Fluids **14**, 1056 (2002); J. M. White and S. J. Muller, Phys. Rev. Lett. **84**, 5130 (2000).

[7] A. Groisman and V. Steinberg, Phys. Rev. Lett. **78**, 1460 (1997).

[8] B. M. Baumert and S. J. Muller, Phys. Fluids **9**, 566 (1997); J. Non-Newtonian Fluid Mech. **83**, 33 (1999).

[9] D. G. Thomas, U. A. Al-Mubaiyedh, R. Sureshkumar, and B. Khomami, J. Non-Newtonian Fluid Mech. (to be published).

[10] R. Sureshkumar, A. N. Beris, and R. A. Handler, Phys. Fluids **9**, 743 (1997).

[11] C. F. Li, B. Khomami, and R. Sureshkumar, J. Non-Newtonian Fluid Mech. (to be published).

[12] P. A. Stone, F. Waleffe, and M. D. Graham, Phys. Rev. Lett. **89**, 208301 (2002).

[13] R. F. Bird, C. F. Curtiss, R. C. Armstrong, and O. Hassager, *Dynamics of Polymeric Liquids* (Wiley, New York, 1987), Vol. 2.